

Three-dimensional seismic model of crustal structure in Southern Norway

B. Loidl,¹ M. Behm,^{2,3} H. Thybo⁴ and W. Stratford^{4,5}

¹Department of Geodesy and Geoinformation, Vienna University of Technology, Vienna, Austria. E-mail: ben.loidl@gmx.at

²Department of Meteorology and Geophysics, University of Vienna, A-1010 Vienna, Austria

³Department of Geophysics, Colorado School of Mines, 1500 Illinois St, Golden, CO 80401, USA

⁴Department of Geology and Geography, University of Copenhagen, Copenhagen, Denmark

⁵Department of Earth Sciences, Durham University, Durham and Stockton-on-Tees, England, UK

Accepted 2013 November 20. Received 2013 November 20; in original form 2013 June 12

SUMMARY

New insights in crustal structure in southern Norway are given by combining stacking techniques and traveltimes tomography of 3-D wide-angle reflection/refraction data. The Magnus Rex crustal scale wide-angle refraction/reflection data set in Southern Norway covers an area of 400 km × 430 km where 716 receivers on three profiles recorded seismic waves from 26 explosive sources. Previous data analysis focused on 2-D interpretation along the profiles. Here we extract additional *P*-wave velocity information by inverting inline and cross-line data simultaneously. We combine stacking routines, traveltimes tomography, and interpolation algorithms to the high quality inline and cross-line data. A smooth 3-D crustal velocity model is inverted from traveltimes of diving Pg waves with similar results for two initial models. Initial models include a 1-D average model and an interpolated 3-D model based on robust, local 1-D velocity-depth functions derived from CMP-sorted and stacked records. The depth to Moho is determined from reflected waves (*PmP*) by traditional exploration seismology processing routines (CMP sorting, NMO correction, stacking, depth conversion). We find that this combination of stacking methods and traveltimes tomography is well suited to exploit sparse 3-D wide-angle data. The results along the profiles are similar to the earlier 2-D models and the 3-D velocity model shows little lateral variation. The crust in SW Norway is generally 35–40 km thick and has relatively low average velocity, as it lacks the characteristic high-velocity lower crust, otherwise observed in the Baltic Shield. However, the Oslo Graben is characterized by high crustal velocities and a slightly elevated Moho. Our results suggest that this crustal structure continues towards the north along the strike of the graben.

Key words: Composition of the continental crust; Controlled source seismology; Seismic tomography; Continental tectonics: extensional; Europe.

1 INTRODUCTION

1.1 The Magnus Rex project

Recent interest in the processes that form and develop topography around the North Atlantic Ocean (e.g. Japsen & Chalmers 2000; Anell *et al.* 2009) has led to new seismic data acquisition in southern Norway within the framework of the MAGNUS (e.g. Weidle *et al.* 2010; Maupin *et al.* 2013) and the Magnus Rex (Stratford *et al.* 2009) projects. The primary objectives of the Magnus Rex project were to determine a well-constrained model of the seismic structure and crustal thickness in southern Norway with the aims of testing if crustal isostasy may explain the existence of the high Norwegian mountain chains and to constrain the velocity structure of the Oslo Rift. This crustal scale wide-angle refraction/reflection

(WAR/R) experiment was carried out in 2007 October. Three seismic profiles were acquired across southern Norway (Fig. 1). The central Southern Scandes Mountains were targeted by two crossing profiles across the highest elevation in the area. A third east–west directed profile crosses both the Southern Scandes and the Oslo Graben (Fig. 1). Vertical component (Texan) seismographs were deployed at 716 stations with a nominal spacing of 2 km along the profiles. Along a 120-km long section across the Oslo graben, the station spacing was decreased to 750 m in order to obtain a high-resolution image of the rift structure. All stations recorded seismic waves from all 26 sources (explosions from 100–400 kg charges in boreholes) providing coverage of crustal structure both along and between the three main profiles.

The recording geometry has a sparse 3-D layout, similar to several other recent WAR/R (Wide-Angle Reflection/Refraction) surveys

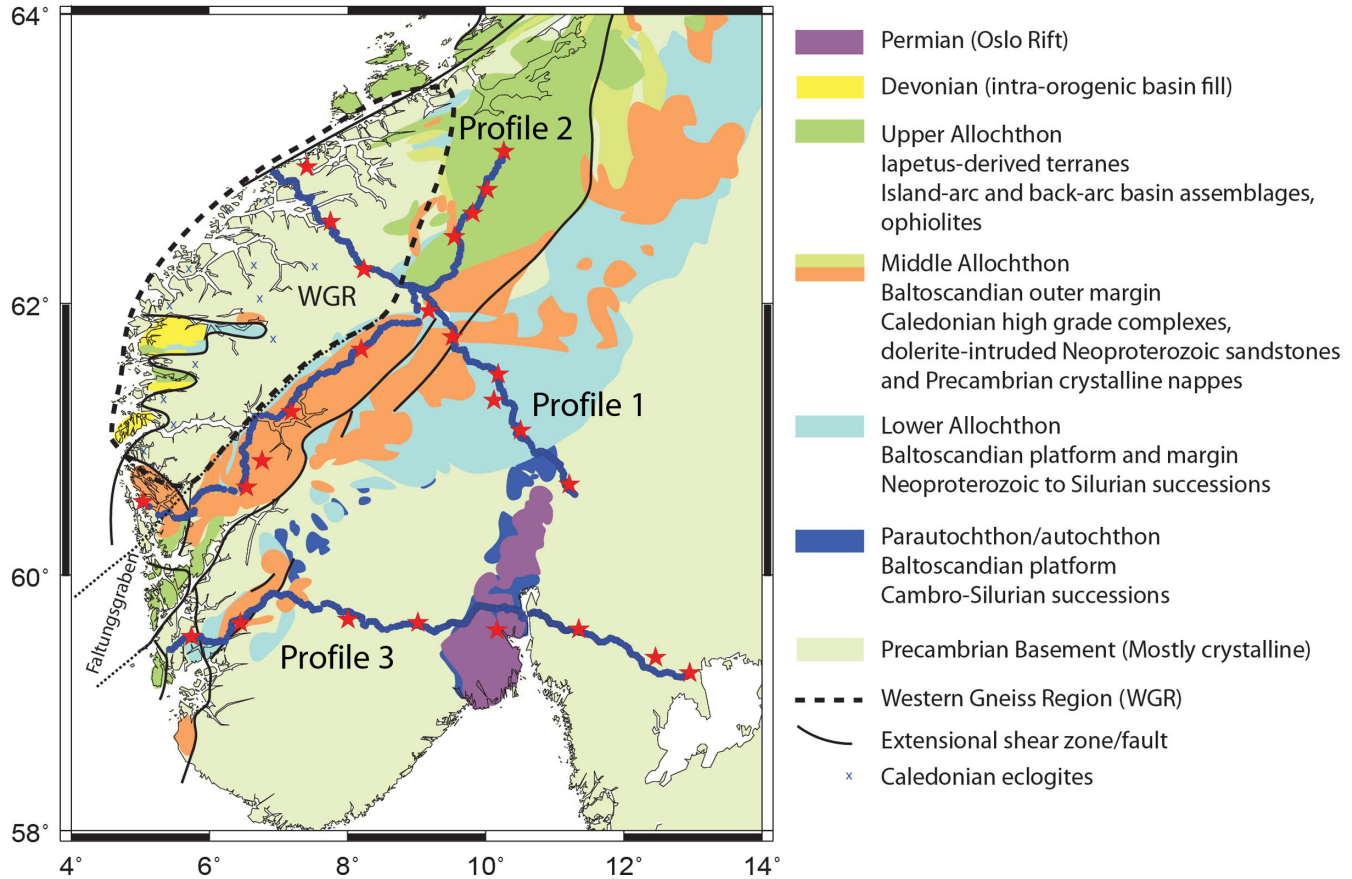


Figure 1. Geologic map and location of shots (red stars) and receivers (blue dots).

that have been conducted within the last decades (e.g. Guterch *et al.* 2003). 3-D processing of WAR/R data is mostly based on tomographic inversion of traveltimes from refracted and reflected waves. A requirement for the application of traveltime tomography is good ray coverage, which is not always fulfilled, particularly with sparse data sets. Behm *et al.* (2007) introduced stacking techniques for WAR/R data to derive robust 3-D models from sparse data at the expense of resolution. Here, we apply these techniques to the Magnus Rex data to gain new insights on the crustal structure of southern Norway, along and between the 2-D recording profiles. We also apply traditional 3-D tomographic inversion methods based on traveltimes. As the cross line coverage is low, even in terms of WAR/R data, we do not anticipate deriving a full 3-D model. Instead we supplement already existing 2-D interpretations, which are used to validate our results.

In general, the combined effect of a large receiver spacing, attenuation and complicated crustal structures can make phase correlation difficult, in particular on cross-line observations. The stacking methods include the entire data set and do not distinguish between inline and cross-line observations, which improves correct phase identification and correlation. However, stacking inherently leads to simplification of the data and resulting models. The trade-off between improved phase correlation and model simplification depends on the recording geometry and the seismic structure in the investigated region. The Magnus Rex data set is relatively sparse, but previous investigations demonstrate a high signal-to-noise (S/N) ratio, which is related to a predominately homogenous crust.

1.2 Geology and tectonic setting

Basement rock of present day southern Norway is part of the Southwest Scandinavian Domain, (Fig. 1) the youngest part of the Fennoscandian Shield, which formed by accretion of terranes to an Archean core in the northeastern parts of Finland and Russia (Gaal & Gorbatshev 1987). The largest part of the Fennoscandian Shield is the centrally located Palaeoproterozoic Svecofennian domain to the east of southern Norway, where several seismic images of collisional structures have shed light on the accretionary processes (e.g. BABEL Working Group 1990; Abramovitz *et al.* 1997). It is mainly composed of highly metamorphosed, 2–1.75 Ga plutonic crust flanked to the west by the Transcandinavian Igneous belt. This series of 1.85–1.65 Ga alkaline and calcic batholiths formed in continental arc settings (Lindh & Gorbatshev 1984). The formation of the Fennoscandian shield was completed by the collision at ~900 Ma between proto-Baltica and an already accreted complex of 1.75–1.5 Ga terranes consisting of plutonic and metamorphic basement that today forms southern Norway (Pesonen *et al.* 1989).

The basement in southern Norway was subsequently affected by the Sveconorwegian (Grenvillian) and Caledonian orogenies (Starmer 1996). The Himalayan style culmination of the Caledonian orogeny was caused by the 440–410 Ma collision between Laurentia and Baltica (e.g. Torsvik *et al.* 1996) when a series of nappe sequences were thrust over Fennoscandian basement. Today most of the basement in southern Norway consists of the lower part of the orogen, which contains material from both the closed Iapetus

Ocean and proto-Baltica (Gee *et al.* 2008). In the central western part of southern Norway, the Western Gneiss Region comprises numerous outcrops of ultra-high pressure, eclogite facies rocks. These rocks were exhumed during the collapse of the Caledonian orogen (Andersen 1998) after having been metamorphosed at depths exceeding 100 km (Hacker *et al.* 2010).

The Oslo Graben formed by rifting by 300 Ma (Heeremans *et al.* 1996) in association with the Variscan orogeny further south (Thybo 2000). Rifting related magmatism continued until 245 Ma (Sundvoll *et al.* 1990). The magma source evolved from an enriched mantle to a progressively depleted source, and the magmatism became dominated by anatexis of previously emplaced material during the late stages of rifting (Neumann *et al.* 2004).

The last major tectonic event that affected southern Norway was the break-up and opening of the North Atlantic Ocean around 55 Ma (e.g. Mosar *et al.* 2002). Long-term stretching preceded break-up and formed a more than 200-km wide stretched continental shelf, which includes a series of deep sedimentary basins extending out to the magmatic continental/oceanic boundary (e.g. Mjælde *et al.* 2009). The effect of the ~40 Ma voluminous magmatism at Iceland and the proposed mantle plume (Vink 1984) on the mantle below the circum-Atlantic landmasses is unclear (e.g. Artemieva & Thybo 2008). Stresses from the ~30 Ma central European Alpine orogeny (e.g. Schmid *et al.* 1996) have affected the basins to the south of Norway, but their effects on the development of topography in Norway is unknown (Anell *et al.* 2009, 2010).

2 SEISMIC DATA AND SIGNAL PROCESSING

A detailed description of the data set is given by Stratford *et al.* (2009). Here we focus on features that are relevant to 3-D processing. *Ca.* 65 per cent of the 18 590 traces are cross-line observations. In general, the S/N ratio of the data is high which is indicative of low attenuation (Fig. 2). While this may indicate that the crust exhibits relatively little scattering and a predominantly homogeneous structure at large scales, Stratford & Thybo (2011a,b) attribute the occurrence of strong *S* waves to inhomogeneities in the uppermost crust. The *Pg* and *PmP* phases are clearly observed in both inline and cross-line record sections, whereas the *Pn* phase is less pronounced. *Pg* waves with apparent velocities ranging from 6.0 to 6.7 km s⁻¹ are detected out to distances of 250 km. In the vicinity of the Oslo Graben, high apparent *Pg* velocities are also obtained at shorter offsets, which suggest high velocities in the middle crust. A total of 1858 *Pg* traveltimes have been manually picked from the single-fold (unstacked) gathers after the application of a bandpass filter (1–2–6–12 Hz) and AGC (window length 5 s; Fig. 3). The average picking accuracy is estimated to be about 0.05 s.

The main energy of the *PmP* phase is concentrated from the critical offset (*ca.* 80 km) out to 150–200 km offset, where its arrival time is close to the arrival times of the *Pg* phase. This leads to difficulties in correct phase identification, in particular on cross-line gathers with small offset variation. This is a major reason for the application of the stacking method, which simplifies the observed wavefield. Due to the large receiver spacing compared to the dominant wavelength, we cannot expect constructive interference of the wavelets. Thus, we apply the envelope function (modulus of the analytical signal) to the data. The STA/LTA algorithm (short-time average to long-time average; Astiz *et al.* 1996) aims to increase the amplitude of the signal. Behm *et al.* (2007) and Behm (2009) demonstrate that the S/N ratio of wide-angle data may be

significantly improved by this method, and we apply the algorithm to the envelope data. The lengths of the windows depend on the frequency content and the time difference between different phases. Optimum results are achieved with window lengths of 45 ms and 1800 ms, respectively. Overall we find only minor improvements by the STA/LTA algorithm, and we consider this as another indication for a generally high S/N ratio of the data.

3 PROCESSING OF *Pg* WAVES

Processing of *Pg* waves aims to derive a smooth 3-D velocity model of the crust. We follow routines that have been successfully applied to 3-D WAR/R data of the Eastern Alps (Behm *et al.* 2007; Behm 2009). A robust 3-D velocity model is obtained from stacked *Pg* phases, and this model is further refined by 3-D traveltome tomography based on picks derived from the original (single-fold) record sections.

3.1 Stacking and inversion of stacked data

Following Behm *et al.* (2007), we construct local 1-D velocity models and interpolate them into a 3-D velocity model. This initial 3-D model is referred to as the *stacking model* v_{st} . The local 1-D velocity models are derived by inverting local 1-D common mid-point (CMP) *Pg* traveltome curves that are picked from offset-bin (OFB) stacks. The OFB stacks and thus the 1-D velocity models are specified on a regular grid with 20-km lateral spacing. The stacks are generated from the signal-processed data set (Section 2). These data are offset-limited to 250 km, and traces without significant *Pg* energy are visually detected and excluded. The remaining 9904 traces are CMP-sorted to cells centred at the gridpoints. The cell size is variable such that each cell contains a minimum number of 30 traces within an offset range of 0–150 km. Depending on the ray coverage, cells may overlap. The average cell size is 24.3 km, and the average cell fold is 175.

The following processing steps are then performed for each cell:

(1) Static corrections are applied to increase the coherency of the *Pg* phases by removing traveltome variations due to near surface structure. The static corrections are derived from a delay-time map based on 701 single-fold *Pg* traveltome picks from within the offset range of 30–90 km. Due to the absence of sedimentary basins, the delay times are small (0.1–0.25 s). Each trace is shifted up by the sum of the delay times at the source and receiver locations, and is eventually shifted down by twice the delay time at the gridpoint. This procedure aims to replace the near surface structure at the source and receiver locations by the near surface structure at the gridpoint.

(2) The traces are arranged by absolute offset and are shifted to align the *Pg* phase. While Behm *et al.* (2007) and Behm (2009) perform the time shift by a linear moveout (LMO) with an average crustal velocity, we account for both the moderate upper crustal velocity and significantly higher velocities in the middle and lower crust. Thus, after a LMO correction with 6 km s⁻¹, we additionally shift the traces by an empirical time–offset relation, which is obtained from a third-order regression polynomial function through the single-fold *Pg* traveltomes (Fig. 3).

(3) Stacking is performed in 5-km OFBs. A mean smoothing filter with a length of 0.5 s is applied to the stacked traces. The offset of each stacked trace is calculated from the average of the absolute offsets of the input traces within each bin. After stacking, the time shift accounting for high velocity in the middle and lower

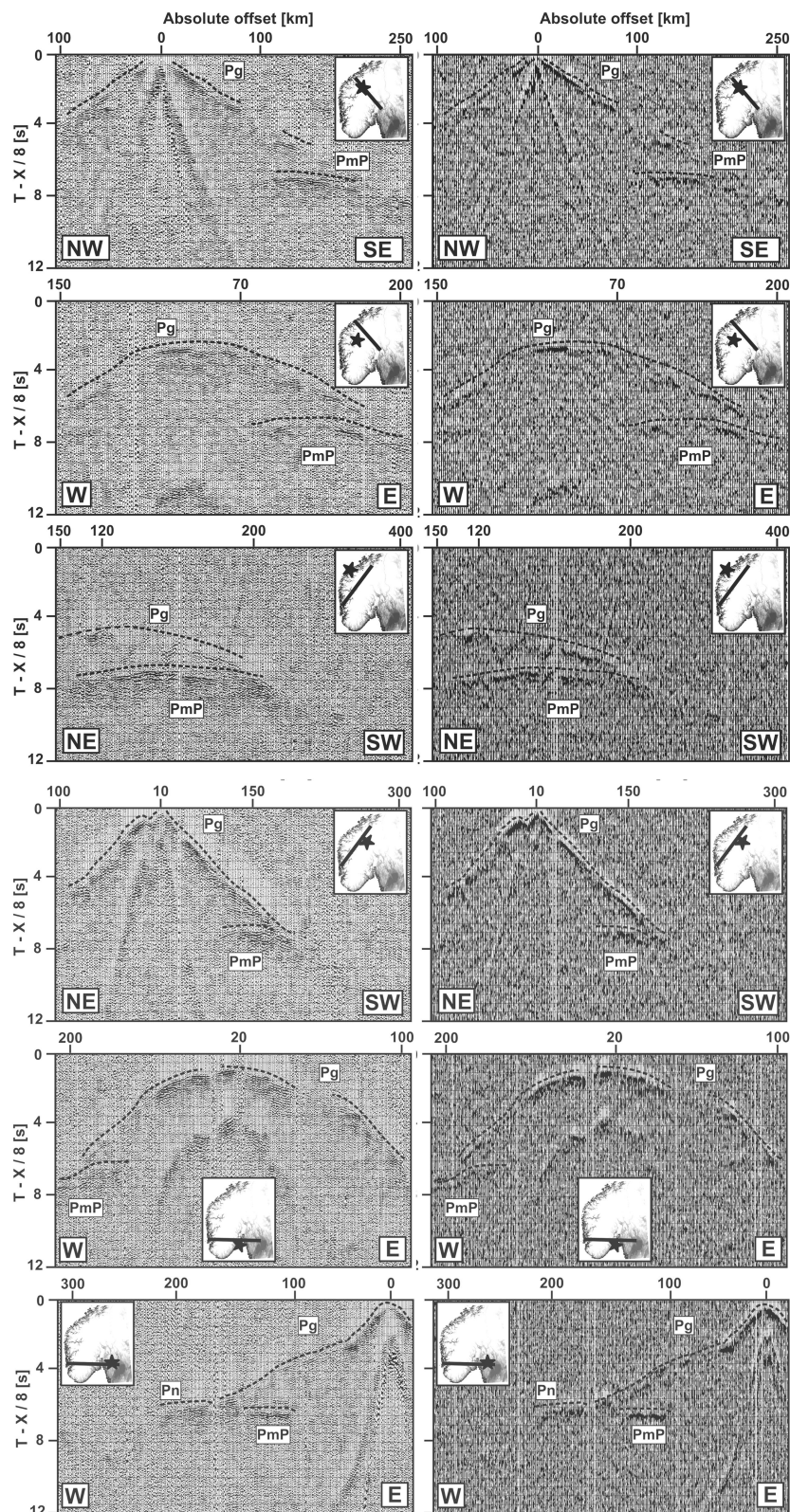


Figure 2. Selected inline and cross-line shot sections. Left column: Application of bandpass filter and AGC. Right column: Additional application of reflection strength and the STA/LTA algorithm. The inlet gives the location of the profile and the shot. The main crustal phases (*Pg*, *PmP*, *Pn*) are indicated by dashed lines.

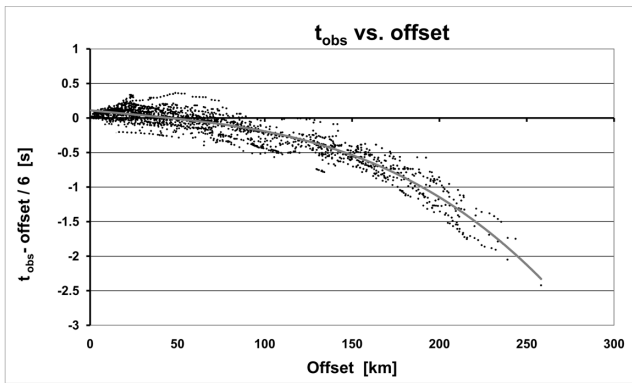


Figure 3. LMO-reduced picked P_g traveltimes from inline and cross-line sections ($n = 1858$). The grey line is a best-fitting third-order polynomial function, which is used for additional time corrections prior to stacking.

crust (step 2) is reversed. Examples of OFB stacks are shown in Fig. 4.

(4) Smooth traveltime curves are picked from the OFB stacks. Due to pre- and post-stack processing, the true onset of the P_g

phase is not clearly defined in the stack. We overcome this problem by superimposing CMP-sorted single-fold traveltime picks on the OFB stack. By this comparison, we find that on average the onset is roughly represented by the first zero-crossing of the stacked wavelet.

(5) The traveltime curve is inverted for a velocity-depth function by an iterative algorithm based on singular value decomposition (Behm *et al.* 2007). Velocities are specified at depth nodes with a vertical spacing of 1 km down to a depth of 15 km, and progressively coarser spacing in the lower crust. Individually weighted smoothing conditions guarantee a stable inversion in case of a low number of traveltime picks. The initial model for the 1-D traveltime inversion is calculated from smoothing and averaging the velocity models given by Stratford *et al.* (2009).

By the steps outlined above, we derive 1-D velocity–depth functions $v_{St}(z)$ at 260 gridpoints. Each velocity–depth function is assigned to the centre (x_b, y_b) of a cell, which is calculated from the average of the CMP locations of all traces in the cell. Thus, the stacking model represents a discrete 3-D velocity model, $v_{St}(x_b, y_b, z)$.

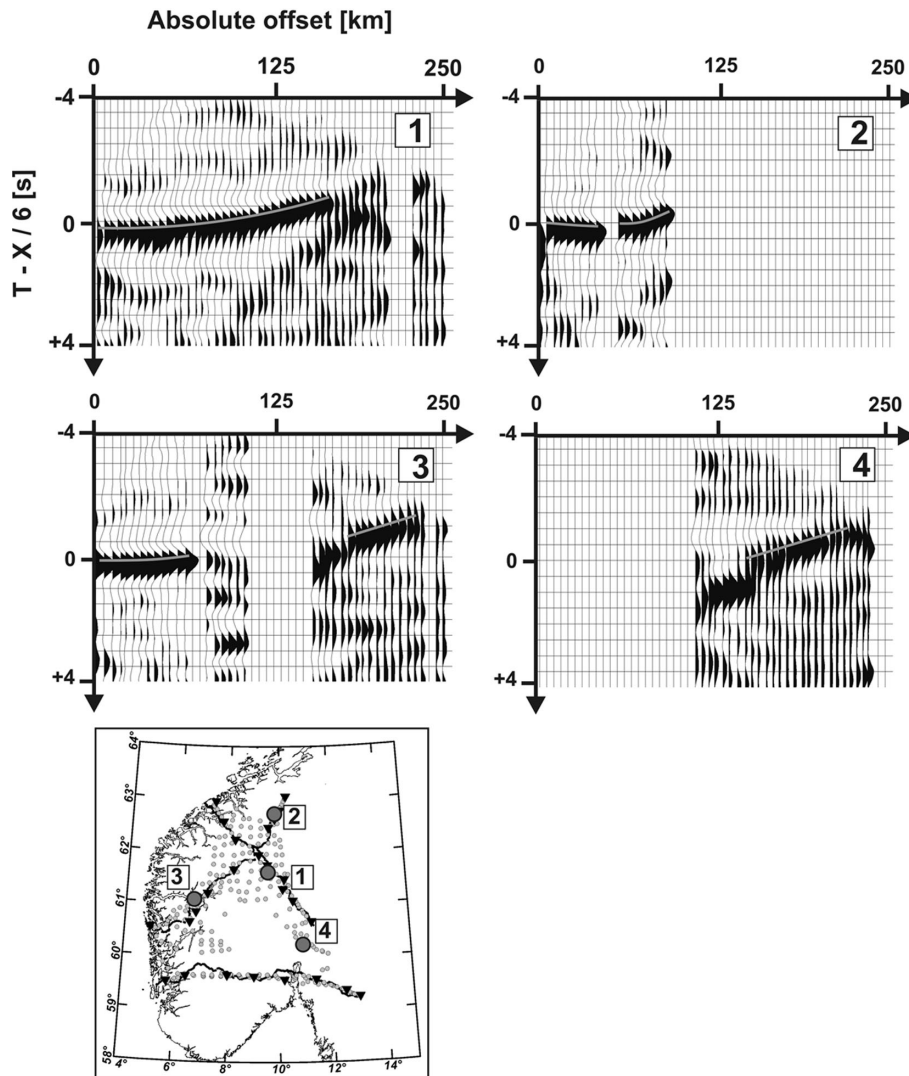


Figure 4. Selected OFB-stacks, displayed with a LMO-correction of 6 km s^{-1} . The line indicates the picked traveltime curves. Black triangles: Location of shots. Light grey circles: Centres of all inverted OFB stacks (= location of the corresponding 1-D velocity-depth functions).

3.2 3-D tomography of single-fold traveltimes

The 1858 single-fold Pg traveltimes (Fig. 3) are used in tomographic inversion for a 3-D velocity model $v_T(x, y, z)$ based on the algorithm by Hole (1992). Starting from an initial model, synthetic Pg ray paths and traveltimes are calculated. The differences to the observed traveltimes are inverted for velocity perturbations along the ray paths by a back-projection technique. The velocity perturbations are smoothed and are added to the initial model to derive an updated velocity model. The whole procedure is iteratively repeated until a satisfactory fit is achieved between the observed and synthetic traveltimes, as expressed by their RMS error. In order to build the velocity model from top to bottom, Pg traveltimes are initially restricted by their offset, and the offset limit is increased stepwise.

The choice of the initial model may be important for the resulting model, in particular if the number of traveltime picks is small. Like Behm *et al.* (2007), we use two different initial models. The first one has variation with depth only (1-D), and velocities are based on the same average function as used for the 1-D inversion in the previous section. The second initial model is a 3-D model, which is interpolated from the stacking model $v_{St}(x_b, y_b, z)$. We refer to the results of these two inversions as $v_{1T}(x, y, z)$ and $v_{3T}(x, y, z)$, respectively. The dimension of the velocity model is $490 \text{ km} \times 460 \text{ km} \times 50 \text{ km}$ with a cell spacing of $1 \text{ km} \times 1 \text{ km} \times 1 \text{ km}$ size. The small spacing is required for the accurate forward calculation of ray paths and traveltimes, which is based on finite differences (Vidale 1990). Smoothing of velocity perturbations is performed by a moving average filter with different length along lateral and vertical axes; however, the model itself is not smoothed.

Both models are similar with respect to the traveltime residuals (Fig. 5, Table 1), and the obtained velocities differ only locally.

Using the stacking model as an initial model, the tomographic inversion also acts as a calibration since the stacking model may include small systematic shifts due to pre- and post-stack signal processing (Behm *et al.* 2007). Comparison of the tomographic and the stacking models shows that the latter is on average too slow in the upper crust and too fast in the middle crust, but by relatively small amounts of 50 m s^{-1} . There is a more pronounced discrepancy in the lower crust (depths $> 30 \text{ km}$), but it must be noted that the coverage at this depth range is low. This discrepancy can be attributed to pick errors on the stacks at large offsets and to a signal-processing induced bias since Pg waves at larger offsets have lower frequency.

The result from tomography has a higher coverage in the lower crust and a lower coverage in the upper crust than the stacking model (Fig. 6). We attribute this difference to previous applications of the stacking procedure to relatively high velocities in the lower crust and a generally homogeneous crustal structure, which minimizes scattering and attenuation. The low coverage in the upper crust may be explained by the sparse shot and receiver layout. Nevertheless, the different 3-D velocity models derived by stacking and 3-D traveltime tomography are in agreement. The two tomographic models calculated from different initial models are remarkably similar. Their slightly different coverage (e.g., at 7 km depth) is explained by the sparse geometry, which makes the inversion more sensitive to the starting model and therefore less stable. The two velocity models diverge in a small region in the northern part of the study area where v_{3T} shows an inversion zone in the upper and middle crust. As this is not indicated by the data, we regard it as an inversion artefact and choose v_{1T} instead of v_{3T} for further processing.

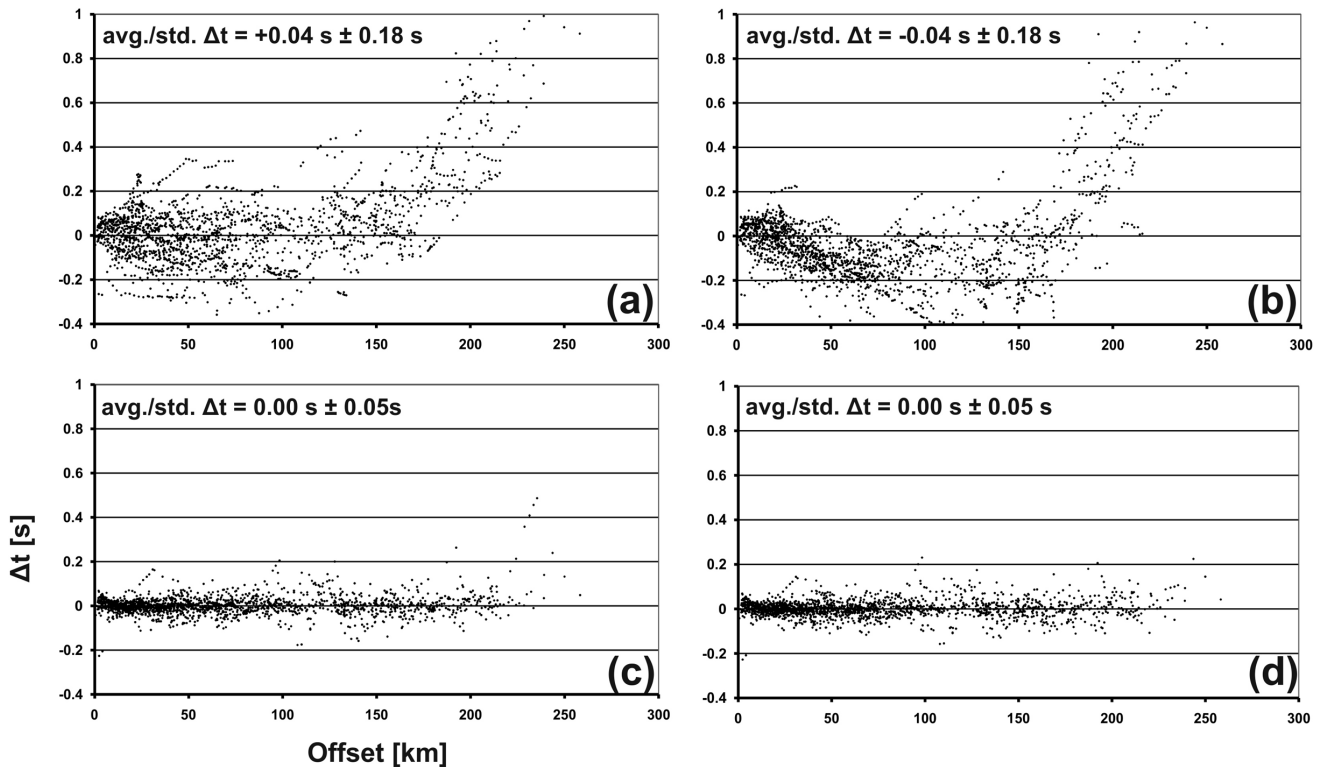


Figure 5. Traveltime residuals Δt before and after the tomographic inversion of the 1858 Pg travel as calculated with the code by Vidale (1990). std., avg.: standard deviation and mean of traveltime residuals. (a) Residuals for the 1-D model. (b) Residuals for the interpolated stacking model $v_{St}(x, y, z)$. (c) Residuals of the model $v_{1T}(x, y, z)$. (d) Residuals of the model $v_{3T}(x, y, z)$. Note that the 1-D model (a) is the initial model for $v_{1T}(x, y, z)$ (c), and that $v_{St}(x, y, z)$ (b) is the initial model for $v_{1T}(x, y, z)$ (d).

Table 1. Inversion parameters and according RMS error of traveltimes residuals for the 3-D tomography of single-fold traveltimes.

Iteration step	Offset limitation (km)	Number of travel times	Smoothing filter size, lateral/vertical (km)	RMS error, v_{1T} (s)	RMS error, v_{3T} (s)
1	80	1158	80/6	0.11	0.11
2	80	1158	40/4	0.07	0.07
3	80	1158	20/2	0.06	0.06
4	80	1158	10/2	0.05	0.05
5	140	1515	80/6	0.07	0.08
6	140	1515	40/4	0.06	0.06
7	140	1515	20/2	0.06	0.06
8	140	1515	10/2	0.05	0.05
9	300	1858	80/6	0.15	0.15
10	300	1858	40/4	0.07	0.08
11	300	1858	20/2	0.05	0.06
12	300	1858	10/2	0.05	0.05

3.3 Final preferred velocity model

The velocity models v_{St} and v_{1T} have different coverage, and a combination of both into a single preferred model facilitates a consistent interpretation. As outlined above, the stacking model v_{St} suffers from small systematic errors due to pre- and post-stack signal processing, and must therefore be calibrated. Behm *et al.* (2007) and Behm (2009) show how calibration and combination of stacking and tomographic models with different coverage can be carried out simultaneously. At each depth level z , the difference $\Delta v(x, y)$ between v_{1T} and v_{St} is calculated at areas of mutual coverage. This difference is then extrapolated to full coverage at each depth level z , and the extrapolated values are added to v_{St} . Extrapolation is carried out by geostatistical methods (Kriging) to avoid overshooting and oscillations of the extrapolated values in case of low coverage (e.g. lowermost crust). The calibrated stacking model is finally combined with v_{1T} where only the latter is available, resulting in a calibrated and final smooth velocity model $v_F(x, y, z)$ (Fig. 7). The standard deviation of the traveltimes residuals calculated with $v_F(x, y, z)$ amounts to 0.11 s.

4 PROCESSING OF WIDE-ANGLE REFLECTIONS (*PmP* WAVES)

The Moho is modelled by stacking of *PmP* phases according to routines established in exploration seismology for steep-angle data (e.g. Yilmaz 2001). The processing flow includes signal processing, trace editing, muting, static correction, CMP sorting, NMO correction, stacking and depth conversion. We refer to Behm *et al.* (2007) for a detailed description of the application to wide-angle data. Here, we focus on the main steps and the specifics of the data set. Although our processing aims to isolate and stack *PmP* waves only, it cannot be ruled out that wide-angle reflections from the lower crust or uppermost mantle also interfere constructively.

4.1 Signal processing, trace editing and muting

We use the same parameters for the pre-stack processing of *PmP* phases as for *Pg* phases (bandpass filter, AGC, envelope; *cf.* Section 2) except for the STA/LTA algorithm. The STA/LTA algorithm is not applied because our objective is to maintain the waveform of the *PmP* reflections, which may contain information on the character of the crust–mantle transition. Also, if *Pg* phases or lower crustal reflections arrive close to the *PmP* phase the STA/LTA

algorithm will enhance the former ones at the cost of the *PmP* phase. Traces without *PmP* energy are detected by visual inspection, and are excluded from further processing. The *Pg* phase is manually muted. Prior to stacking, a mean smoothing filter with a window length of 2 s is applied to the data.

4.2 Lowering of the datum plane

For steep-angle reflection data, static corrections relative to a final datum are mostly based on the assumption of vertical incidence. For wide-angle rays, the horizontal slowness can be large and the inclination of the ray cannot be neglected. Therefore, time corrections will be more precise after lowering the datum plane along the ray, which also invokes a shift of the source and receiver coordinates towards the CMP (Behm *et al.* 2007). This is done under the assumption of a 1-D stratified medium, and the ray parameter is calculated for each source–receiver pair from the average *Pg* velocity $v_F(x, y, z)$ and assumed Moho depths (Stratford *et al.* 2009) at the CMP.

The static corrections are small in southern Norway since the velocity variations in the upper crust are small compared to regions with significant sedimentary basins. However, lowering the datum also implies a shift of the source and receiver coordinates, which in turn leads to an offset reduction. A small offset reduces the uncertainty of the NMO correction (*cf.* Section 4.3), and consequently, the datum should be chosen as deep as possible. Imperfectly known crustal velocities introduce errors in the ray calculation and thus in the time corrections which at some point will outweigh the effect of offset reduction. Based on the coverage of the *Pg* velocity model, we therefore choose a depth of 15 km for the datum. All following procedures are carried out with the data brought down to this level.

4.3 CMP sorting, NMO correction and stacking

After lowering the datum, we find that *PmP* reflections occur between offsets of 40 and 120 km, and restrict the traces used accordingly for further processing. CMP bins are defined on a 10 km \times 10 km spaced grid. The bin size is variable, such that a minimum number of 10 traces are assigned to each bin. The average bin size is 10.5 km, and the average trace fold is 34.

NMO correction has a significant impact on stacking of WAR/R data, since the hyperbolic move-out is largest at large offsets. Thus we compare the results from three different NMO velocity models. The first one is a constant velocity of 6700 m s⁻¹ for each bin.

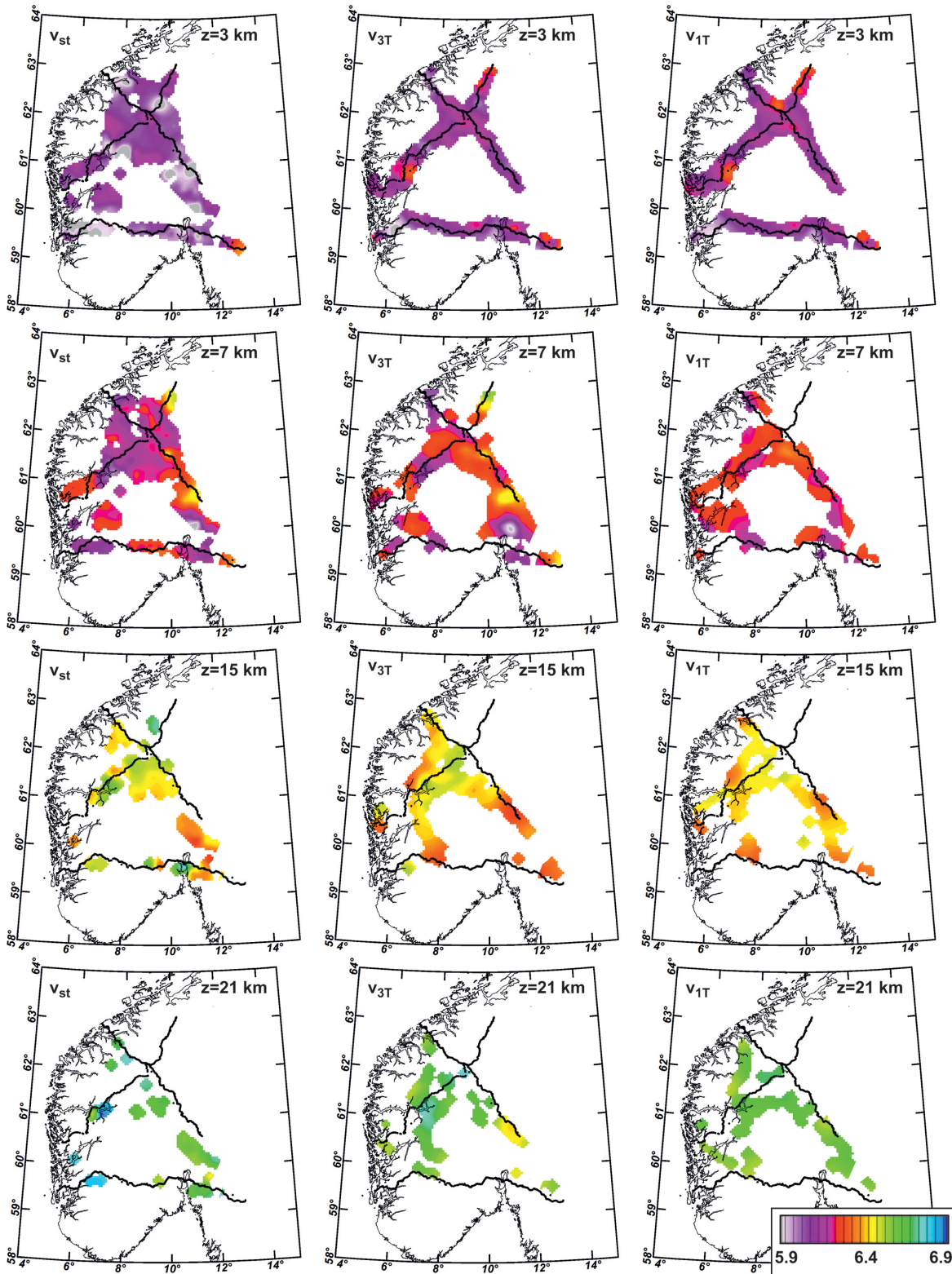


Figure 6. Depth slices through the three velocity models $v_{st}(x, y, z)$, $v_{3T}(x, y, z)$ and $v_{1T}(x, y, z)$.

Model 2 is laterally variable, as the NMO velocity at each bin is calculated from the extrapolated velocity model v_F (Section 3). Model 3 is also laterally variable, and it represents a combination of the models v_{st} and v_{3T} (Section 3). Average values and standard deviations of models 2 and 3 are $6710 \pm 73 \text{ m s}^{-1}$ and $6676 \pm 59 \text{ m s}^{-1}$, respectively. All three models reflect the NMO velocity

between 15 km depth and the Moho depth given by Stratford *et al.* (2009). Comparison shows that the choice of the NMO model has very little effect on the output of the stacking process. We take this as an indication of overall homogeneity of the crustal structure. All three NMO velocity models represent plausible crustal structures of the region, and their little overall variation, in conjunction with

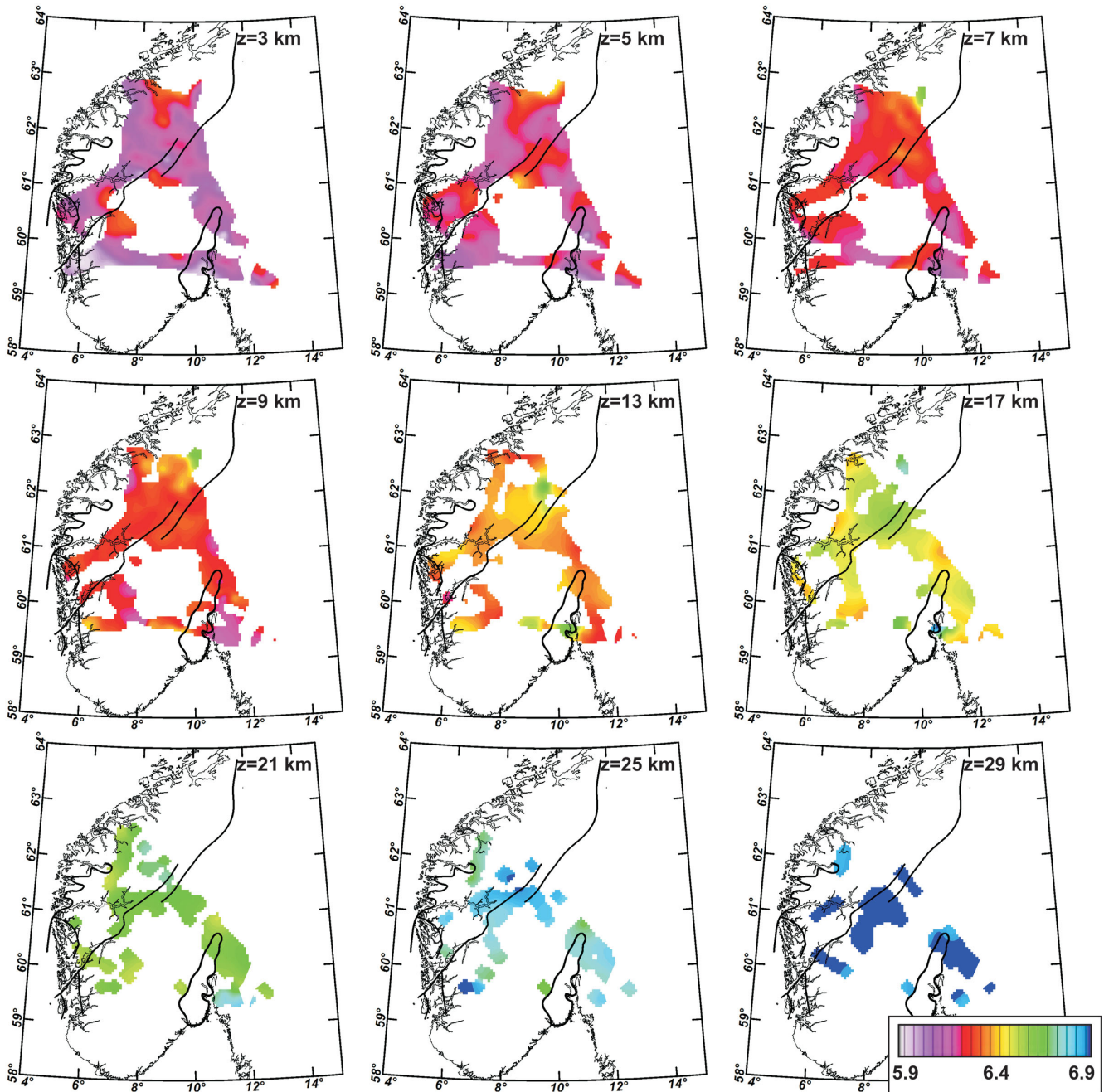


Figure 7. Depth slices through the final velocity model $v_F(x, y, z)$.

lowering the datum plane, explains the stability of the stacks. For the sake of consistency, we use the results obtained with NMO velocity model 2 for further processing.

4.4 Results

The stacks are depth-converted with the velocity model v_F and assigned to the centre of the CMP's of all traces collected into each bin. We do not migrate the data since the inherent simplifications of ray-based WAR/R migration (Behm *et al.* 2007) and the insufficient resolution of the data for migration purposes will outweigh potential improvements, in particular because of the long wavelength variation of the Moho. Slices through the 3-D cube of stacked wide-angle reflections are shown in Fig. 8. In order to increase the S/N

ratio of and sharpen the wavelet, the amplitudes are raised to their 5th power. The patchy appearance of the stacks results from the sparse 3-D coverage. Nevertheless, substantial new cross-line information is gained. Due to pre-processing (envelope calculation) and pre-stack smoothing, it is not clear at this stage of processing which part of the long wavelet represents the depth of the Moho. This question is addressed in the next section.

5 DISCUSSION

We use the results obtained by Stratford *et al.* (2009) and Stratford & Thybo (2011b) to validate the obtained models along the three recording profiles (Figs 9 and 10). Crustal velocity-depth profiles are compared at specific locations (Fig. 9). Despite the different

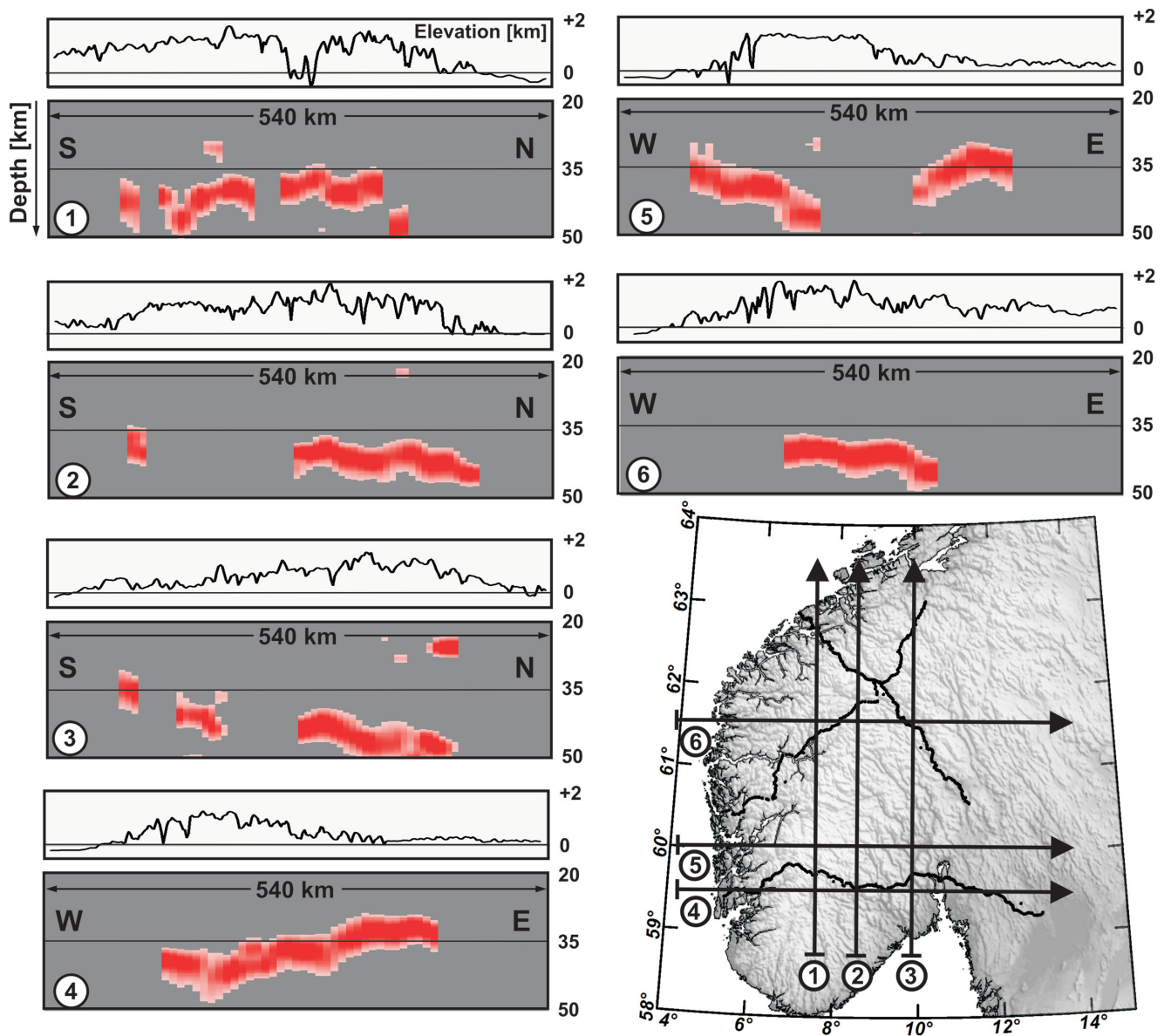


Figure 8. Vertical slices through the cube of stacked and depth converted wide-angle reflections. These stacked reflections are associated with the Moho in most cases, but they can also represent lower crustal reflectors.

parameterization (layers with velocity discontinuities versus smooth variation), we find a good overall agreement. A notable exception is location 3 on profile 2, where 2-D modelling derives higher velocities in the shallow crust (2–7 km depth) than 3-D modelling. However, Stratford & Thybo (2011b) also show that the observed high velocities in the 2-D model are specific to one shot. They relate those velocities to an isolated near-surface block, which may appear too large in the seismic 2-D model. The 3-D model also contains high velocities, but their location is shifted slightly to the northwest (Fig. 7). Additionally, the 3-D model generally includes higher velocities in the middle crust (> 13 km depth) than the 2-D profiles. Due to the additional inclusion of cross-line data in the vicinity of location 3, we regard these velocities as plausible. As already noted by Stratford & Thybo (2011b), our results also indicate that this region of the Caledonides is characterized by anomalous velocity–depth relationships.

Location 5 at the Oslo Graben also shows a difference in the middle crust. The dense receiver spacing in the area increases the

resolution of 2-D modelling, but this advantage may be partially lost during 3-D stacking and tomography because of uniform grid sizes and smoothing parameters. Thus, the 2-D interpretation may be regarded as more plausible, although it is noted that 2-D modelling will be affected by strong curvature of the recording profiles, and the offline location of the shots.

Due to the low-pass filtering and envelope calculation, the stacked and depth-converted reflections represent an approximately 4–5-km wide wavelet, and it is not clear which part of the wavelet (e.g. onset, maximum, bottom) is the best proxy for the Moho. The Moho depths derived by 2-D modelling generally correspond to the onset of the wavelet (Fig. 10). A similar conclusion was made by Behm *et al.* (2007) and Behm (2009) for data from the Alps. Based on this observation, we tentatively pick Moho depths from the onset of the stacks and compare them with the Moho map by Stratford *et al.* (2009). The difference is 0.6 ± 2.7 km. The small mean difference indicates that the identification of the onset of the Moho is reasonably well constrained. Local deviations from this

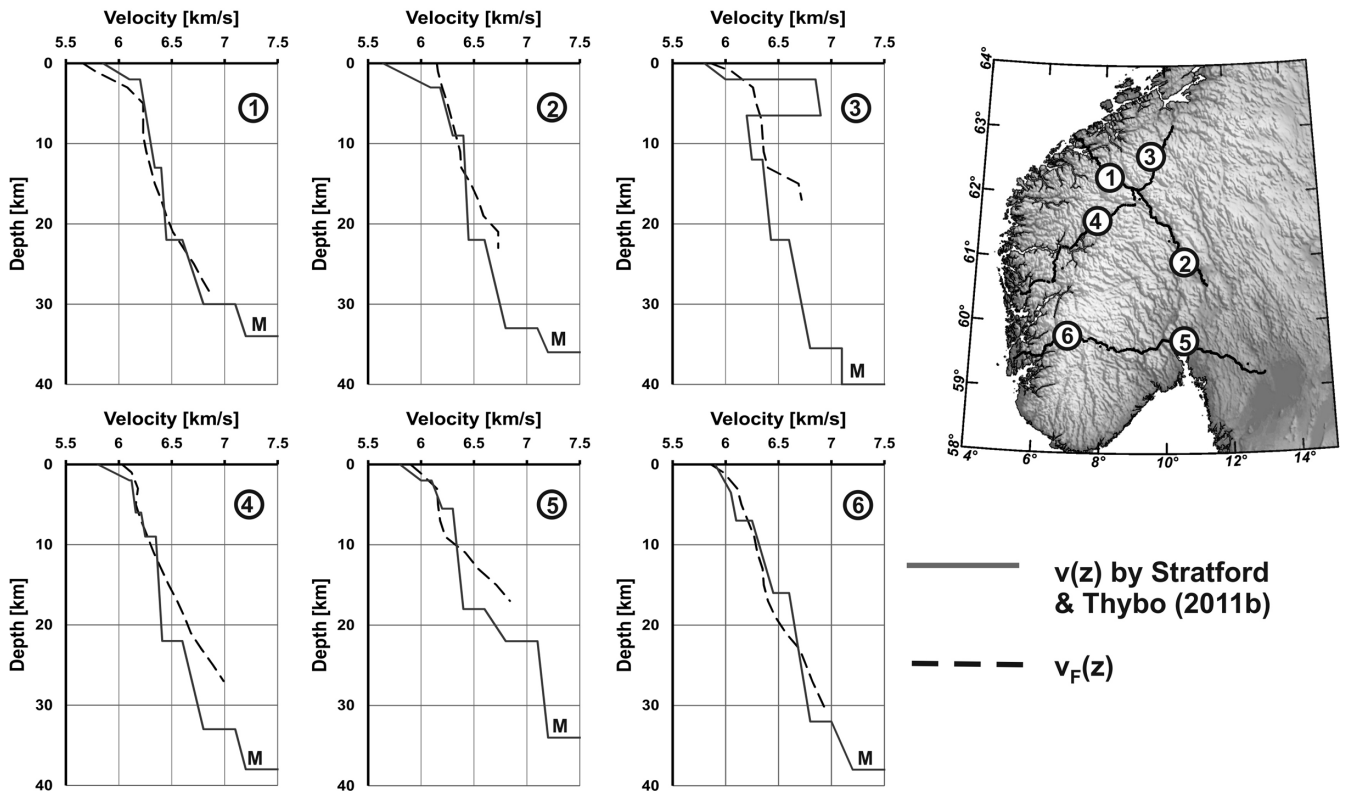


Figure 9. Comparisons between velocity-depth functions obtained from 3-D processing and previous 2-D interpretation (Stratford & Thybo 2011b). M, Moho.

observation are discussed in the next paragraph. We do not construct a new Moho map based on our data since we consider the overall coverage as too low. Accurate Moho depths from stacked WAR/R data also require single-fold Pn or PmP traveltimes for global and local calibration, but those traveltimes were not collected in this study.

At the northern end of profile 1, the stacked wide-angle reflections appear significantly deeper than the Moho obtained from 2-D modelling (Fig. 10a), and thus may suggest a deeper crust–mantle boundary. In the original data, there is a pronounced reflection at an offset range of 80–160 km, which is attributed to a mantle reflector by Stratford *et al.* (2009), although wide-angle reflections from the uppermost mantle at depths of 50–60 km are often strongest at larger offsets (>200 km; e.g. Sřoda *et al.* 2006; Öberseder *et al.* 2011). The 2-D model shows the Moho rise at profile distances 70–120 km where the elevation is highest along the profile. Two additional interpretations have been carried out in this part of the study area. The 2-D model has been extended to the NW into the sea by interpretation of additional seismic refraction data (Kvarven *et al.*, in preparation; Maupin *et al.* 2013). Combining the on- and off-shore data sets shows that the shallow Moho provides a continuous Moho topography along this profile. Further new receiver function interpretation (Frasetto & Thybo 2013) infers Moho depths similar to the shallow Moho in the 2-D model.

Both the 2-D and the 3-D models derive a gently northeastward dipping Moho along profile 2 (Fig. 10b). The discrepancy at the northernmost tip probably could result from a too high NMO velocity in the stacking model, as the depth penetration of the crustal model is poor at this location. However, the receiver function interpretation (Frasetto & Thybo 2013) also indicates that the Moho is deeper than in the 2-D model at this northern tip of the profile, and it is further noted that the 2-D model is not constrained by Pn

refractions at this location. Thus, we favour the 3-D solution at this specific location.

Profile 3 (Fig. 10c) crosses the Oslo Graben at a distance of 250–300 km. The Moho structures of the two interpretations are in agreement in the western part. The onset of the reflection band rises to 29 km depth at a distance of 250–370 km in the 3-D model. This significant bulge does not exist in the 2-D model. The 3-D crustal velocity model has velocities of about 6.7 km s^{-1} at depths as shallow as 15 km directly above the bulge, indicating intrusion of high-velocity material in the middle crust. However, due to lack of coverage of velocities in the deeper crust, the NMO velocity in this area is mainly based on extrapolation from the adjacent regions, resulting in an average NMO velocity of only 6.75 km s^{-1} for the Oslo Graben. On the contrary, the 2-D velocity model indicates thickening of the high velocity ($>7.1 \text{ km s}^{-1}$) lower crust beneath the Oslo Graben. Based on this model and on an older data set (Tryti & Sellevoll 1977), the average velocity between 15 km depth (the datum plane, Section 4.2) and the Moho is about 7.15 km s^{-1} . Thus, the lower NMO velocity of 6.75 km s^{-1} would result in shallower 3-D Moho depths compared to the 2-D model (Fig. 11). The depth difference of stacking phases within the used offset range (40–120 km) with velocities of 6.75 km s^{-1} and 7.15 km s^{-1} , respectively, amounts to 5 km, and thus may explain the elevated 3-D Moho below the Oslo Graben.

Alternatively, the bulge could represent a strong velocity contrast in the lowermost crust instead of the Moho. A velocity contrast from 6.8 km s^{-1} to a high-velocity lower crust ($7.1\text{--}7.4 \text{ km s}^{-1}$) is interpreted at depths between 20 and 28 km in the 2-D model of profile 3 (Stratford & Thybo 2011a). The shape of this velocity discontinuity resembles the bulge, although the latter is shifted to the west by ca. 50 km and is overall deeper. The high-velocity lower crust ($>7.1 \text{ km s}^{-1}$) exists over the entire length of all

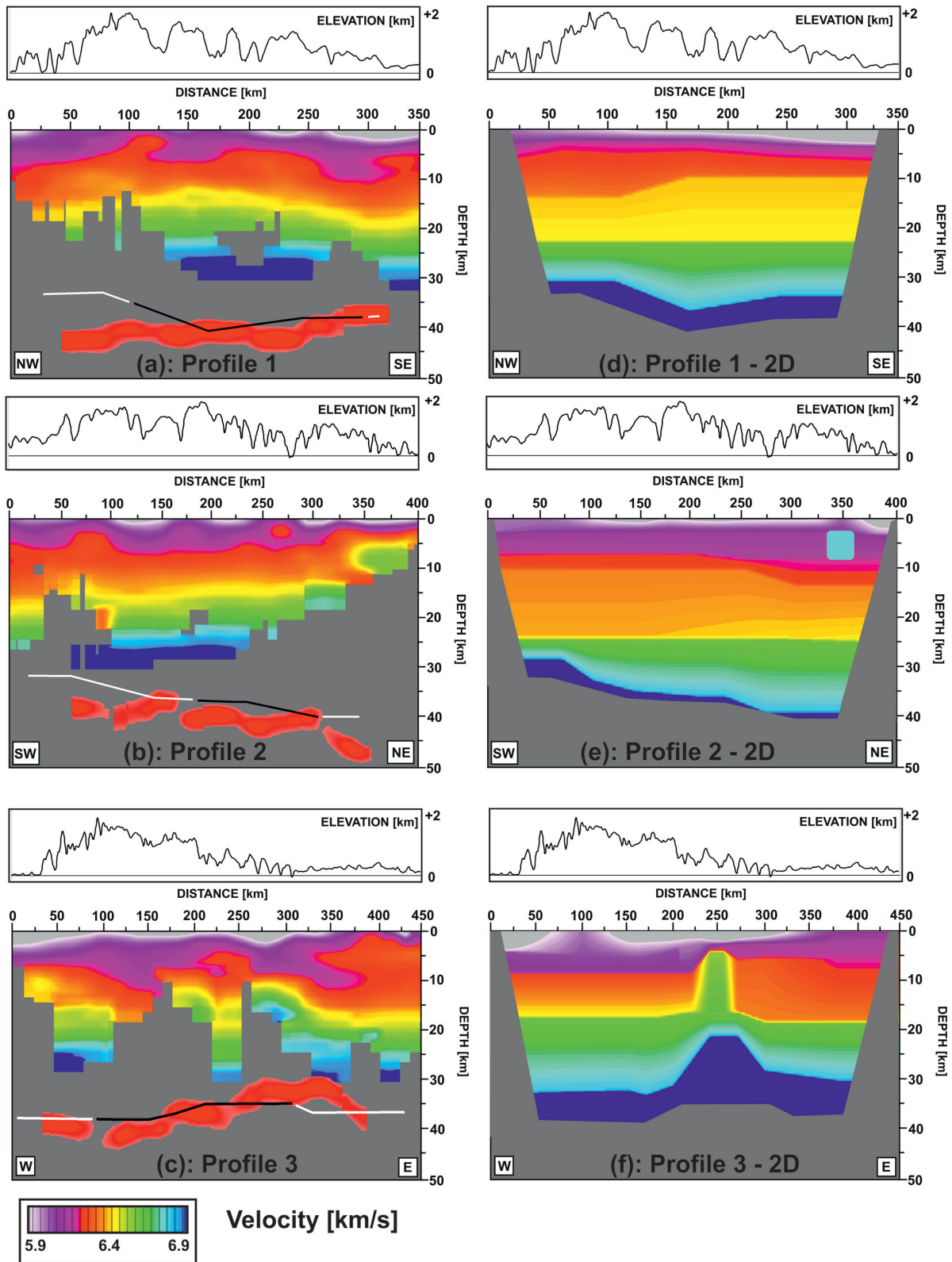


Figure 10. (a)–(c) Comparisons of Moho depths obtained from previous 2-D interpretation (Stratford *et al.* 2009) with depths from 3-D stacking (red reflection band). The black lines indicate Moho depths by Stratford *et al.* (2009), which are constrained by both P_n and P_mP phases, while the white lines are based on P_mP only. The crustal velocity model $v_F(x, y, z)$ is also superimposed. (d)–(f) Crustal velocity models obtained from previous 2-D interpretation (Stratford *et al.* 2009) for comparison with $v_F(x, y, z)$ shown in (a)–(c). The bottom of the crustal velocity models corresponds to the 2-D Moho. Spatial shifts between model features in the 2-D and 3-D models may also be related to geometry issues, since the 2-D profiles are strongly curved. See text for discussion.

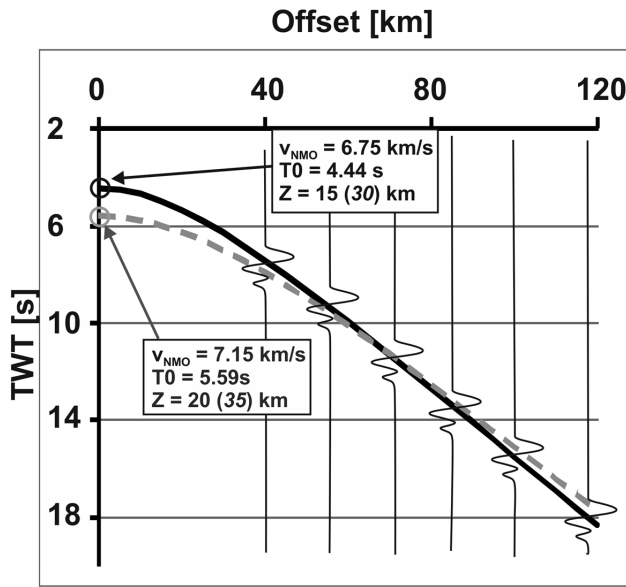


Figure 11. Move-out hyperbolae for NMO velocities of 6.75 and 7.15 km s^{-1} . Depending on the choice of the velocity, phases might stack at 15 or 20 km depth. All values are related to the datum at $z = 15 \text{ km}$. Italic numbers refer to the datum $z = 0 \text{ km}$. The offset range 40–120 km is used for stacking of *PmP* phases. The wavelets are only schematics used for illustration.

2-D profiles, although it is considerably thinner (4–8 km) outside the Oslo Graben. The existence of the high-velocity lower crust in the 2-D models is mainly based *PmP* moveouts and on early exploration data (Tryti & Sellevoll 1977). The hypothesis of the bulge representing the top of the high-velocity lower crust in the Oslo Graben does not explain why the reflection band coincides with the Moho on all other locations. We therefore find it more likely that the bulge results from too low velocities used for NMO correction and depth conversion. We readdress this issue in the next section.

With the exception of the Moho below Oslo Graben, we find a good fit between the 2-D and the 3-D models. It must also be considered that due to topographic and logistic constraints, major parts of the profiles are curved rather than straight. This can lead to inaccuracies in 2-D modelling, where the rays are assumed to travel in a vertical plane. Also, for comparison purposes we sample the 3-D results on a 2-D plane, which deviates up to 20 km from the actual location of the profiles. This is in particular the case in the Oslo Graben along profile 3, where pronounced spatial shifts between 2-D and 3-D model features are observed.

The overall similarity of the 2-D and 3-D models along the profiles adds confidence to the interpretation of the new results. The homogeneity of the crust in Southern Norway is not only indicated by a high S/N ratio of the data, but it is also directly deduced from the 3-D models. The velocities show little lateral variation. Velocities in the mid and lower crust are in the range of $6.5\text{--}6.8 \text{ km s}^{-1}$ throughout the investigated area, indicating the absence of a thick high-velocity cratonic lower crust, as is usually observed in the Baltic Shield further east (e.g. BABEL Working Group 1993a,b). The most pronounced deviation from this rather uniform crustal structure is observed in the Oslo Graben. As outlined above, the observed bulge in the stacked reflections below the Oslo Graben is interpreted as a spuriously shallow Moho resulting from too low crustal velocities used for NMO correction and depth conversion. Cross-line coverage enables us to trace the bulge to the north. We calculate the difference of the top of the bulge to the Moho depth

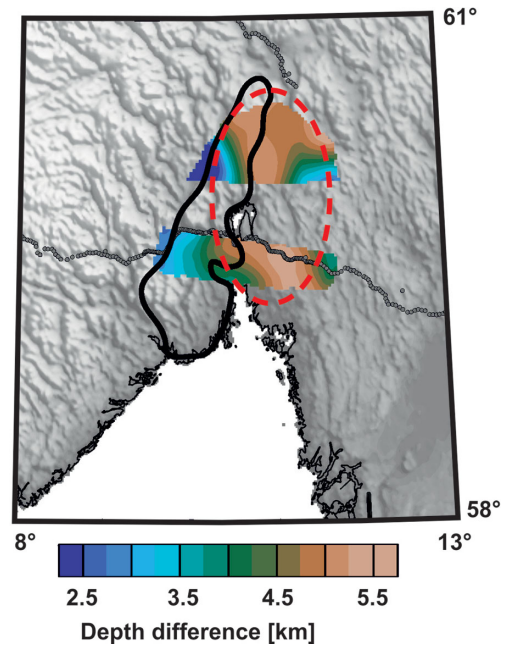


Figure 12. Depth differences between the Moho bulge in the 3-D model and the Moho depth given by Stratford *et al.* (2009). The bulge results from too low NMO velocities in the 3-D model and its extent is used to tentatively estimate the region of high crustal velocities (encircled area).

given by Stratford *et al.* (2009), which results in an approximately 130-km long and 90-km wide feature (Fig. 12). We use the lateral extent and magnitude of this feature as a rough proxy for the area where higher NMO velocities than obtained from the 3-D model prevail. It exhibits an S–N oriented ridge which is shifted to the west with respect to the rift graben and the associated the Permian volcanics as observed in outcrops. This area corresponds to a high velocity lower crust observed in the 2-D models by Tryti & Sellevoll (1977) and Stratford & Thybo (2011a) who interpret it as an underplated layer related to the Permian rifting episode (see also Thybo & Artemieva 2013).

6 CONCLUSIONS

Stacking and inversion techniques are applied to a 3-D WAR/R data set from Southern Norway. As in previous studies, these methods prove to be successful in imaging the large-scale crustal structure and Moho topography. Difficulties in phase correlation on cross-line gathers are avoided by CMP sorting and stacking, thus enabling modelling of the entire data set. In analogy to previous 2-D modelling, we find little lateral variation of the crustal velocities, indicating a uniform crust throughout Southern Norway. A notable exception is the region of the Oslo Graben, where we interpret a North–South trending high-velocity structure in the lower crust.

ACKNOWLEDGEMENTS

We thank the research group geophysics at Technical University of Vienna for providing computational infrastructure and in particular Werner Chwatal and Ewald Brückl for support and discussion. Mariusz Majdański and an anonymous reviewer provided very helpful comments on the manuscript.

REFERENCES

- Abramovitz, T., Berthelsen, A. & Thybo, H., 1997. Proterozoic sutures and terranes in the southeastern Baltic Shield interpreted from BABEL deep seismic data, *Tectonophysics*, **270**, 259–277.
- Andersen, T.B., 1998. Extensional tectonics in the caledonides of southern Norway, an overview, *Tectonophysics*, **285**, 333–351.
- Anell, I., Thybo, H. & Artemieva, I.M., 2009. Cenozoic uplift and subsidence in the North Atlantic region: Geological evidence revisited, *Tectonophysics*, **474**, 78–105.
- Anell, I., Thybo, H. & Stratford, W., 2010. Relating Cenozoic North Sea sediments to topography in southern Norway: The interplay between tectonics and climate, *Earth planet. Sci. Lett.*, **300**, 19–32.
- Artemieva, I. & Thybo, H., 2008. Deep Norden: highlights of the lithospheric structure of Northern Europe, Iceland, and Greenland, *Episodes*, **31**, 98–106.
- Astiz, L., Earle, P. & Shearer, P., 1996. Global stacking of broadband seismograms, *Seismol. Res. Lett.*, **67**, 8–18.
- BABEL Working Group, 1990. Evidence for early Proterozoic plate tectonics from seismic reflection profiles in the Baltic Shield, *Nature*, **348**, 34–38.
- BABEL Working Group, 1993a. Deep seismic reflection/refraction interpretation of crustal structure along BABEL profiles A and B in the southern Baltic Sea, *Geophys. J. Int.*, **112**, 325–343.
- BABEL Working Group, 1993b. Integrated seismic studies of the Baltic Shield using data in the Gulf of Bothnia region, *Geophys. J. Int.*, **112**, 305–324.
- Behm, M., 2009. 3-D modelling of the crustal S-wave velocity structure from active source data: application to the Eastern Alps and the Bohemian Massif, *Geophys. J. Int.*, **179**, 265–278.
- Behm, M., Brückl, E., Chwatal, W. & Thybo, H., 2007. Application of stacking and inversion techniques to 3D wide-angle reflection and refraction seismic data of the Eastern Alps, *Geophys. J. Int.*, **170**, 275–298.
- Frasetto, A. & Thybo, H., 2013. Receiver function analysis of the crust and upper mantle in Fennoscandia—ostostatic implications, *Earth planet. Sci. Lett.*, **381**, 234–246.
- Gee, D.G., Fossen, H., Henriksen, N. & Higgins, A.K., 2008. From the early Paleozoic platforms of Baltica and Laurentia to the Caledonide orogen of Scandinavia and Greenland, *Episodes*, **31**, 44–51.
- Gaal, R. & Gorbatshev, R., 1987. An outline of the Precambrian evolution of the Baltic shield, *Precamb. Res.*, **35**, 15–52.
- Guterch, A., Grad, M., Špicák, A., Brückl, E., Hegedüs, E., Keller, G.R., Thybo, H. & CELEBRATION 2000. ALP2002, SUDETES 2003 Working Groups, 2003. An overview of recent seismic refraction experiments in Central Europe, *Stud. Geophys. Geod.*, **47**, 651–657.
- Hacker, B.R., Andersen, T.B., Johnston, S., Kylander-Clark, A.R.C., Peterman, E.M., Walsh, E.O. & Young, D., 2010. High-temperature deformation during continental-margin subduction & exhumation: the ultrahigh-pressure Western Gneiss Region of Norway, *Tectonophysics*, **480**, 149–171.
- Heeremans, M., Larsen, B.T. & Stel, H., 1996. Paleostress reconstruction from kinematic indicators in the Oslo Graben, Southern Norway; new constraints on the mode of rifting, *Tectonophysics*, **266**, 55–79.
- Hole, J.A., 1992. Nonlinear high-resolution three-dimensional seismic travel time tomography, *J. geophys. Res.*, **97**, 6553–6562.
- Japsen, P. & Chalmers, J.A., 2000. Neogene uplift and tectonics around the North Atlantic: overview, *Global planet. Change*, **24**, 165–173.
- Lindh, A. & Gorbatshev, R., 1984. Chemical variation in a protorecric suite of granitoids extending across a mobile belt–craton boundary, *Geologische Rundschau*, **73**, 881–893.
- Maupin, V. et al., 2013. The deep structure of the Scandes and its relation to tectonic history and present-day topography, *Tectonophysics*, **602**, 15–37.
- Mjelde, R., Faleide, J.I., Breivik, A.J. & Raum, T., 2009. Lower crustal composition and crustal lineaments on the Vøring Margin, NE Atlantic: a review, *Tectonophysics*, **472**, 183–193.
- Mosar, J., Lewis, G. & Torsvik, T.H., 2002. North Atlantic sea-floor spreading rates: implications for the Tertiary development of inversion structures of the Norwegian-Greenland Sea, *J. Geol. Soc.*, **159**, 503–515.
- Neumann, E.-R., Wilson, M., Heeremans, M., Spencer, E.A., Obst, K., Timmerman, M.J. & Kirstein, L., 2004. Carboniferous–Permian rifting and magmatism in southern Scandinavia, the North Sea and northern Germany: a review. Permian–Carboniferous Magmatism and Rifting in Europe, *Geol. Soc. London. Spec. Publ.*, pp. 11–40.
- Öberseder, T., Behm, M., Kovacs, I. & Falus, G., 2011. A seismic discontinuity in the upper mantle between the Eastern Alps and the Western Carpathians: constraints from wide angle reflections and geological implications, *Tectonophysics*, **504**, 122–134.
- Pesonen, L.J., Torsvik, T.H., Elming, S.A. & Bylund, G., 1989. Crustal evolution of Fennoscandia; palaeomagnetic constraints, *Tectonophysics*, **162**, 27–49.
- Schmid, S.M., Pfiffner, O.A., Froitzheim, N., Schonborn, G. & Kissling, E., 1996. Geophysical-geological transect and tectonic evolution of the Swiss-Italian Alps, *Tectonics*, **15**, 1036–1064.
- Sfoda, P. et al., 2006. Crustal and upper mantle structure of the Western Carpathians from CELEBRATION 2000 profiles CEL01 and CEL04: seismic models and geological implications, *Geophys. J. Int.*, **167**, 737–760.
- Starmer, I.C., 1996. Oblique terrane assembly in the late paleoproterozoic during the Labradorian-Gothian Orogeny in southern Scandinavia, *J. Geol.*, **104**, 341–350.
- Sundvoll, B., Neumann, E.R., Larsen, B.T. & Tuen, E., 1990. Age relations among Oslo rift magmatic rocks—implications for tectonic and magmatic modeling, *Tectonophysics*, **178**, 67–87.
- Stratford, W. & Thybo, H., 2011a. Crustal structure and composition of the Oslo Graben, Norway, *Earth planet. Sci. Lett.*, **304**, 431–442.
- Stratford, W. & Thybo, H., 2011b. Seismic structure and composition of the crust beneath the southern Scandes, Norway, *Tectonophysics*, **502**, 364–382.
- Stratford, W., Thybo, H., Faleide, J.I., Olesen, O. & Tryggvason, A., 2009. New Moho Map for onshore southern Norway, *Geophys. J. Int.*, **178**, 1755–1765.
- Thybo, H., 2000. Crustal structure and tectonic evolution of the Tornquist Fan region as revealed by geophysical methods, *Bull. Geol. Soc. Denmark*, **46**, 145–160.
- Thybo, H. & Artemieva, I.M., 2013. Moho and magmatic underplating in continental lithosphere, *Tectonophysics*, in press.
- Torsvik, T.H., Smethurst, M.A., Meert, J.G., Van, d.V.R., McKerrow, W.S., Brasier, M.D. & Walderhaug, H.J., 1996. Continental break-up and collision in the Neoproterozoic and Palaeozoic; a tale of Baltica and Laurentia, *Earth-Sci. Rev.*, **40**, 229–258.
- Tryti, J. & Sellevoll, M.A., 1977. Seismic crustal study of the Oslo Rift, *Pure appl. Geophys.*, **115**(4), 1061–1085.
- Vidale, J.E., 1990. Finite-difference calculation of travel times in three dimensions, *Geophysics*, **55**, 521–526.
- Vink, G.E., 1984. A hotspot model for Iceland and the Vøring plateau, *J. geophys. Res.*, **89**, 9949–9959.
- Weidle, C. et al., 2010. MAGNUS—a seismological broadband experiment to resolve crustal and upper mantle structure beneath the Southern Scandes Mountains in Norway, *Seismol. Res. Lett.*, **81**, 76–84.
- Yilmaz, Ö., 2001. *Seismic Data Analysis*, 2nd edn. Society of Exploration Geophysicists.